



Article

Insight into the Contributions of Surface Oxygen Vacancies on the Promoted Photocatalytic Property of Nanoceria

Yuanpei Lan ^{1,2} , Xuewen Xia ^{1,2}, Junqi Li ^{1,2,*}, Xisong Mao ^{1,2}, Chaoyi Chen ^{1,2,*}, Deyang Ning ^{1,2}, Zhiyao Chu ^{1,2}, Junshan Zhang ^{1,2} and Fengyuan Liu ^{1,2}

- ¹ Department of Metallurgical Engineering, College of Materials and Metallurgy, Guizhou University, Huaxi, Guiyang 550025, China; yplan@gzu.edu.cn (Y.L.); XuewenXiaCN@outlook.com (X.X.); gz-maoxisong@outlook.com (X.M.); ndy1113@gmail.com (D.N.); ZhiyaoChuCN@outlook.com (Z.C.); JunshanZhangCN@outlook.com (J.Z.); FengyuanLiu-CN@outlook.com (F.L.)
- ² Guizhou Province Key Laboratory of Metallurgical Engineering and Process Energy Saving, Guiyang 550025, China
- * Correspondence: jqli@gzu.edu.cn (J.L.); ccy197715@126.com (C.C.); Tel.: +86-13594152275 (J.L.); +86-15086015817 (C.C.)

Abstract: Oxygen vacancies (OVs) have critical effects on the photoelectric characterizations and photocatalytic activity of nanoceria, but the contributions of surface OVs on the promoted photocatalytic properties are not clear yet. In this work, we synthesized ceria nanopolyhedron (P-CeO₂), ceria nanocube (C-CeO₂) and ceria nanorod (R-CeO₂), respectively, and annealed them at 600 °C in air, 30%, 60% or pure H₂. After annealing, the surface OVs concentration of ceria elevates with the rising of H₂ concentration. Photocatalytic activity of annealed ceria is promoted with the increasing of surface OVs, the methylene blue photodegradation ratio with pure hydrogen annealed of P-CeO₂, C-CeO₂ or R-CeO₂ is 93.82%, 85.15% and 90.09%, respectively. Band gap of annealed ceria expands first and then tends to narrow slightly with the rising of surface OVs, while the valence band (VB) and conductive band (CB) of annealed ceria changed slightly. Both of photoluminescence spectra and photocurrent results indicate that the separation efficiency of photoinduced electron-hole pairs is significantly enhanced with the increasing of the surface OVs concentration. The notable weakened recombination of photogenerated carrier is suggested to attribute a momentous contribution on the enhanced photocatalytic activity of ceria which contains surface OVs.



Citation: Lan, Y.; Xia, X.; Li, J.; Mao, X.; Chen, C.; Ning, D.; Chu, Z.; Zhang, J.; Liu, F. Insight into the Contributions of Surface Oxygen Vacancies on the Promoted Photocatalytic Property of Nanoceria. *Nanomaterials* **2021**, *11*, 1168. <https://doi.org/10.3390/nano11051168>

Academic Editor:
Diego Cazorla-Amorós

Received: 27 March 2021
Accepted: 27 April 2021
Published: 29 April 2021

Publisher's Note: MDPI stays neutral with regard to jurisdictional claims in published maps and institutional affiliations.



Copyright: © 2021 by the authors. Licensee MDPI, Basel, Switzerland. This article is an open access article distributed under the terms and conditions of the Creative Commons Attribution (CC BY) license (<https://creativecommons.org/licenses/by/4.0/>).

Keywords: surface oxygen vacancies; nanoceria; photocatalytic property; band gap; photoinduced carriers

1. Introduction

Cerium is the first element in the periodic table to possess a ground state electron in a 4f orbital (Xe 4f¹5d¹6s²), which is responsible for the powerful redox behavior between its two ionic states, Ce⁴⁺ (the Xe ground state) and Ce³⁺ (Xe 4f¹) [1]. Cerium dioxide is known for its excellent redox ability, outstanding oxygen storage capacity and stable chemical properties, which make ceria a prominent function material for various applications, e.g., three-way catalysis [2], water gas shift reaction (WGS) [3,4], solar energy conversion [5,6], gas sensor [7] and chemical-mechanical polishing [8]. Meanwhile, nanoceria is also employed as one of the most attractive photocatalysts for environmental applications [9,10], clean energy generation [11,12], CO₂ utilization [13–15], etc.

It is generally accepted that the photocatalytic application of ceria is impeded by its wide band gap ~3.2 eV and a quick recombination of photogenerated electrons (e⁻) and holes (h⁺) [16,17]. Attributing to the redox characteristic of Ce⁴⁺/Ce³⁺ pairs, oxygen vacancy is an inescapable topic for researching on ceria based catalysts [1,18,19]. Oxygen vacancies (OVs) or Ce³⁺ have been reported to affect both band structure and recombination of photocarriers significantly, and promote the photocatalytic activity of ceria [20–23]. It is believed that the OVs are favorable for reducing the e⁻/h⁺ pairs recombination rate [24,25].

Band gaps of ceria are mostly reported to be narrowed after more OV's generated [20,21,26], while a few researchers, e.g., Gao et al. [22] found the ceria with a higher OV's concentration had a blue-shift of light absorption. The existing divergent influence of OV's on ceria band gap may be interrelated to the concentration, distribution or location of OV's in ceria lattice. Though, the ceria containing more OV's shows a higher photocatalytic activity under the same light source [20–22,26], then the contributions of OV's on the enhanced photocatalytic property of ceria is unclear.

Reduction of the stoichiometric CeO₂ is a main way to enrich OV's concentration in ceria lattice, including CO or H₂ reducing [22,27,28], X-ray/UV/Ar⁺/plasma exposing [29–34] or a high temperature annealing [35]. Reducing ratio of ceria by H₂ primarily depends on H₂ concentration and reduction temperature, while surface oxygen may be taken away by H₂ at a low temperature [36]. The subsurface or bulk oxygen of ceria would react with H₂ molecules and depart away over around 850 °C, and tends to form Ce₂O₃ [37]. Annealing the ceria at a same temperature for the same length of time with a different concentration reductant, e.g., H₂, is a facile way to produce ceria samples with a surface OV's concentration gradient.

Moreover, different morphologies of ceria mainly expose diverse crystal faces, where the typical morphologies including polyhedral, cubic and rod-like shape of nanoceria primarily expose the (111), (100) and (110)/(100) plane, respectively [38,39]. It is suggested that the (111) is the most stable face, and OV's are most easily formed on the (100) but which would be partially oxidized due to high surface activity, and a higher concentration of surface OV's normally exist on (110) plane [40–42]. The effects of OV's on the photoelectric characterizations of various shaped ceria may be different, and which still need to be systematically studied.

Thus, in present work, we synthesized polyhedral, cubic and rod-like shape of nanoceria, and annealed them at 600 °C in air, 30%, 60% or pure H₂ to obtain ceria with various surface OV's concentration. The effects of the surface OV's on band structure, photogenerated carriers, and photocatalytic activity of different shapes of nanoceria are carefully discussed.

2. Materials and Methods

2.1. Materials

Cerium nitrate hexahydrate (Ce(NO₃)₃·6H₂O, 99.95%) and sodium hydroxide (NaOH, 99.9%) were purchased from Aladdin Chemistry Co. Ltd. (Shanghai, China), which were used as received without further purification. The H₂ and Ar gas with the purity of 99.999% were ordered from Shen-Jian Co., Guiyang, China.

2.2. Synthesis Process

Nanoceria was synthesized by using a simple template-free hydrothermal method under a variety of conditions to modify the morphology, which was similar to the synthetic route reported in Ref. [43]. Briefly, NaOH aqueous solutions were dropwise added into Ce(NO₃)₃·6H₂O aqueous solution to form light purple mixtures with strong stirring for 30 min and then transferred to a 50 mL Teflon stainless steel autoclave, which would be maintained at a designed temperature for 24 h. More synthetic conditions are listed in Table S1. After the autoclave cooling down, all products were washed and filtered with distilled water and alcohol several times to remove impure ions, followed by drying at 60 °C in air overnight. The obtained polyhedral, cubic, and rod-like nanoceria are named as raw P-CeO₂, C-CeO₂ and R-CeO₂, respectively.

2.3. Annealing Process

The raw P-CeO₂, C-CeO₂ and R-CeO₂ were placed in a ceramic boat and then maintained in a tube furnace (gsl-1600×, Kejing, Hefei, China) for 2 h annealing at 600 °C with a heating rate of 10 °C/min under air, 30, 60 or 100% H₂ atmosphere, respectively. Before a H₂ annealing process, air was repeatedly expelled from the furnace tube by alternately flowing argon and vacuuming for several times. The total gas flow rate was 400 mL/min

and argon was selected as the balance gas (88.79 kPa total pressure of Guiyang), and the annealed powders were henceforth named as P-CeO₂-X, C-CeO₂-X and R-CeO₂-X (X = air, 30% H₂, 60% H₂ or H₂).

2.4. Subsection Analysis

The obtained powders were subjected to several analyses. X-ray powder diffraction pattern was recorded by using X-Pert Powder (Panalytical, The Netherlands) with Cu K α radiation ($\lambda = 0.15418$ nm) from 5.00 to 90.00° at a rate of 0.02°/s. Micrographs were taken by SEM (JSM 7610, JEOL, Tokyo, Japan) and TEM (Tecnai G2 F20, FEI, Hillsboro, OR, USA) in which the samples were ultrasonically dispersed in alcohol and dropped on the silicon wafer or copper grid. TG analysis was recorded by Mettler TGA/SDTA 851e at a heating rate of 10 °C/s from room temperature to 1000 °C with the air and 30%, 60% and pure H₂, where Ar was used as carrier gas. H₂-TPR was analyzed by AutoChem1 II 2920, 0.1000 \pm 0.0005 g of sample was kept at 500 °C in the air for 1 h and cooled down to room temperature. After 30 min purification in Ar at room temperature, the sample was heated to 1000 °C with the mixed gas of 10% H₂ and 90% Ar with a total gas flow of 30 mL/min and a heating rate of 10 °C/min. X-ray photoelectron spectroscopy (XPS) was recorded by K-Alpha (Thermo Fisher Scientific, Waltham, MA, USA), in which a monochromatic Al source ($h\nu = 1486.6$ eV) and the samples were tested in a vacuum situation of 2×10^{-9} mbar with C 1s peak (284.8 eV) reference. The UV-visible diffuse reflectance spectra (UV-Vis DRS) were recorded by UV 2700 (Shimadzu, Tokyo, Japan) with the wavelength from 200 to 800 nm and BaSO₄ was used as reference, while the photoluminescence spectroscopy (PL spectra) was analyzed by FluoroMax-4 (HORIBA, France) with an excitation wavelength of 300 nm. The ultraviolet photoelectron spectroscopy (UPS) recording by ESCALAB 250Xi (Thermo Fisher, Waltham, MA, USA) was performed the valence states of all samples at the He I line ($h\nu = 21.2$ eV) with C 1s reference in a vacuum situation of 2×10^{-8} mbar. Transient photocurrent curves were recorded under a light irradiation provided by a 250 W xenon lamp in 0.1 mol/L Na₂SO₄ aqueous solution at bias voltage of 0.4 V, which was employed by an electrochemical workstation (CHI660C, CHI shanghai Co., Shanghai, China) in three electrode cells. The tested samples were dispersed in a nafion (10 μ L), ethanol (750 μ L) and deionized water (750 μ L) mixture solution and further dip-coated on a glassy carbon plate ($\Phi = 3$ mm), which was used as the working electrode, and a Pt plate and Ag/AgCl were employed as the counter and reference electrode, respectively. The BET surface area and N₂ adsorption results were analyzed by ASAP2460 (Micromeritics, Norcross, GA, USA).

2.5. Photocatalytic Performance

The photocatalytic performances were tested by a self-built photochemical reactor, which was composed of a 250 W xenon lamp and a quartz vessel. In total, 80 mL of methylene blue (MB) solution with a concentration of 10 mg/L was used for simulating the waste dye solution, and 20 mg of synthesized catalyst was added into the reactor with ultrasound for 10 min. After 30 min of dark adsorption, the lamp was turned on and the catalyst was reacted with the MB under a light facula, 5 mL solution was sampled for 30 min each in the next 2 h. The sampled solution was centrifuged firstly with a speed of 10,000 r/min for 5 min and then the MB concentration was measured by a spectrophotometer under the maximum wavelength of 664 nm. The degradation ratio can be calculated by the following formula [44,45]:

$$\text{Degradation ratio (\%)} = (C_0 - C_i)/C_0 \times 100\%. \quad (1)$$

At a low concentration of MB with a weak adsorption, the photocatalytic reaction kinetics in general follow the Langmuir–Hinshelwood (L-H), and the equation of the pseudo-first-order reaction rate constant [46] can be given as:

$$\ln(C_i) = -kt + \ln(C_0), \quad (2)$$

where C_0 and C_i are the initial and tested concentration of MB, respectively, k is the pseudo-first-order reaction rate constant (min^{-1}), t is the photocatalytic reaction time (min).

3. Results and Discussion

3.1. Phase and Morphology

XRD patterns of synthesized nanoceria are exhibited in Figure 1, it can be seen that all samples show the typical diffraction peaks of CeO_2 with a fluorite-type structure and $\text{Fm}\bar{3}\text{m}$ space group (PDF: #03-065-2975). The raw C- CeO_2 has the strongest diffraction intensity, followed by raw P- CeO_2 and R- CeO_2 , the crystal sizes of raw P- CeO_2 , raw C- CeO_2 and raw R- CeO_2 were calculated as 6.7, 36.5, and 10.0 nm, respectively.

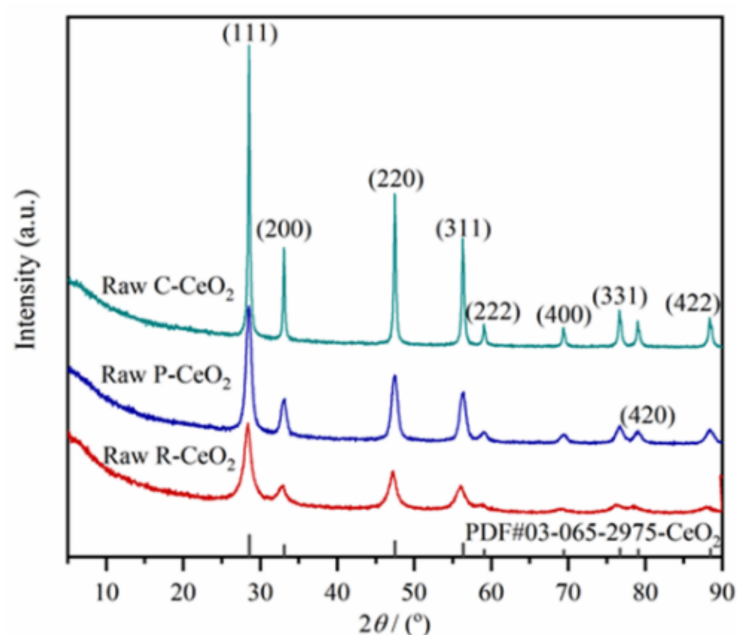


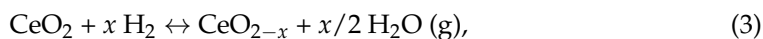
Figure 1. XRD patterns of raw P- CeO_2 , C- CeO_2 and R- CeO_2 .

In Figure 2, TEM images clearly exhibit that the synthesized nanoceria samples own the desired morphology of polyhedron, cube and rod, the counted statistical particle size of synthesized ceria is given in Figure S1, showing the average size of P- CeO_2 , C- CeO_2 and R- CeO_2 is around 9, 40, and 100 nm (for length), respectively. From the HRTEM images as shown in Figure 2, the spacing lattice fringes are measured as 0.318 and 0.321 nm for the P- CeO_2 associating with presenting (111) plane, and the (100) face is found in the HRTEM image of C- CeO_2 , while both (110) and (100) planes are exposed in the R- CeO_2 , which is in agreement with the theory for the main exposing face of various shaped ceria [38].

3.2. Reduction of Ceria in H_2

The TG analysis results of raw R- CeO_2 under different atmospheres are shown in Figure 3a, obviously weight loss can be found under each atmosphere and the weight loss increases in a higher H_2 concentration atmosphere. In air condition, the first weight loss is about 5.6 wt. % corresponding to the vaporization of free water, then the R- CeO_2 continues to weightlessness from 138 to 356 °C, where the weight loss is about 3.2 wt. %, which may be in connection with the $\text{Ce}(\text{OH})_4$ decomposition [47]. At a higher temperature, the weight signal of sample stabilizes at about 89.0 wt. % of initial weight. The weight loss of ceria in 30%, 60% or pure H_2 atmosphere can be divided into four steps: (i) free water evaporation; (ii) H_2 adsorbs on the surface of R- CeO_2 and hydroxylates with Ce^{4+} accompanying by the water decomposing [48], which leads to around 2.9, 4.2 and 5.7 wt. % of weightlessness at 356 °C under different hydrogen concentration; (iii) the surface of R- CeO_2 is continually and incompletely reduced by H_2 , and the decrement of weight is

about 1.7 wt. % at 837 °C for 30% H₂, 2.0 wt. % at 782 °C for 60% H₂, and 6.0 wt. % at 757 °C for pure hydrogen atmosphere, respectively; (iv) the subsurface of ceria is reduced and tends to form Ce₂O₃ [37]. With the increasing of H₂ concentration, the weight loss of raw R-CeO₂ at the same temperature increases, which means more O atoms are divorced from ceria lattice by the following reaction:



where $0 < x < 0.5$, and nonstoichiometric value of x depends on the temperature and H₂ partial pressure.

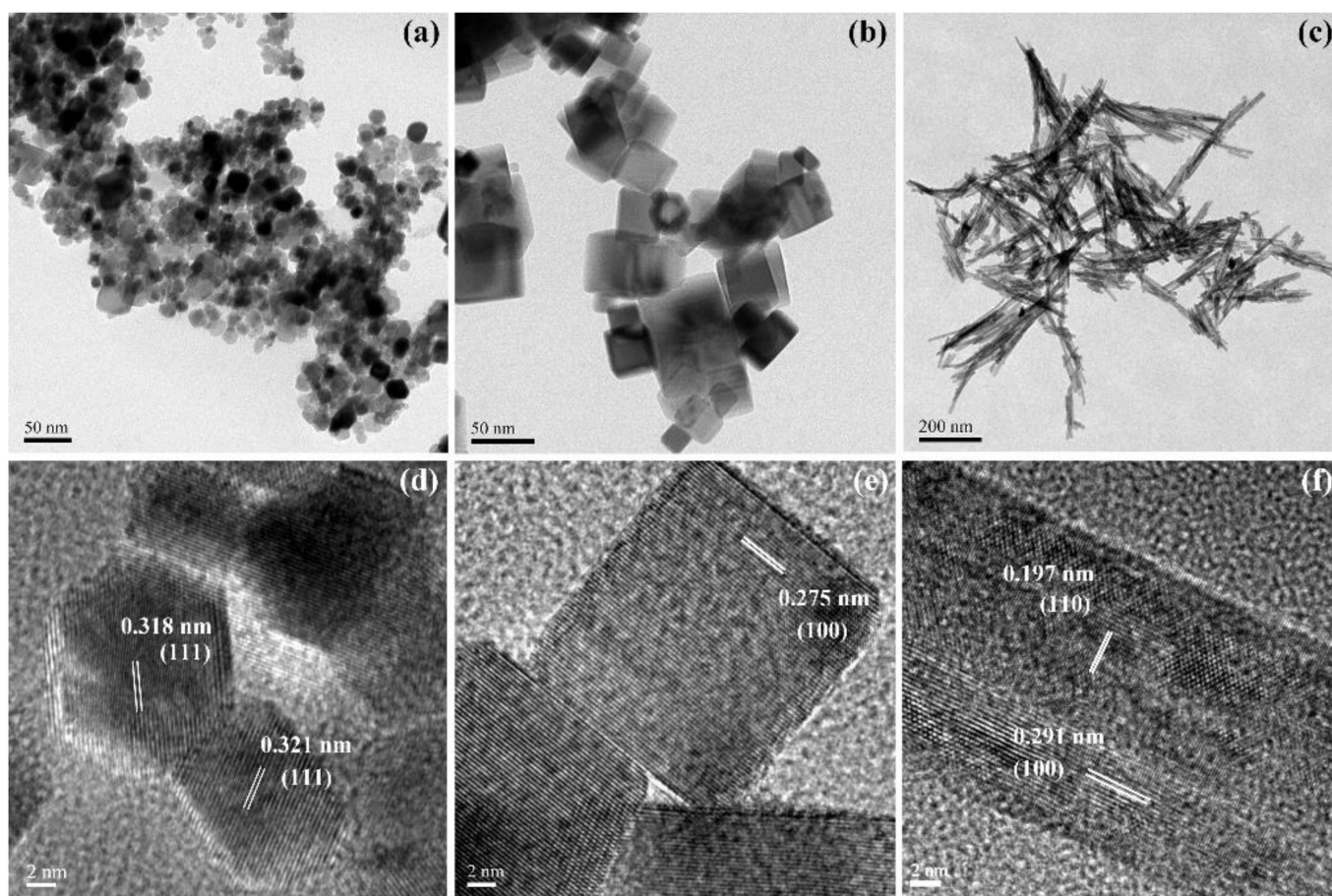


Figure 2. TEM images of raw P-CeO₂ (a), C-CeO₂ (b) and R-CeO₂ (c), HRTEM images of raw P-CeO₂ (d), C-CeO₂ (e) and R-CeO₂ (f).

The H₂-TPR results of synthesized raw CeO₂ are shown in Figure 3b. The first and second peak shown in TPR curves corresponds to the surface reduction and bulk reduction of ceria by hydrogen, respectively [36]. The synthesized various structural nanoceria samples show different start/end reduction temperatures for the first reduction stage of three tested samples, where R-CeO₂ has the widest reduction range of 254.1–501.9 °C, P-CeO₂ shows the narrowest range from 360.1 to 485.8 °C, followed by the 271.9–492.0 °C for C-CeO₂. At the second reduction step, the maximum reduction peaks are found to be achieved at the temperature of 758.8, 776.4 and 787.7 °C for C-CeO₂, R-CeO₂ and P-CeO₂, respectively. The notable diversity of the reducing behavior for the R-CeO₂, C-CeO₂ and P-CeO₂ further verifies the different activities of the mainly exposed crystal faces in ceria, where (110) and (100) are more active than (111) facet [40,41,49,50]. Based on the TG and H₂-TPR results, annealing ceria at a same temperature of 600 °C in different hydrogen

partial pressure atmosphere will produce ceria samples with various concentration of surface OV's.

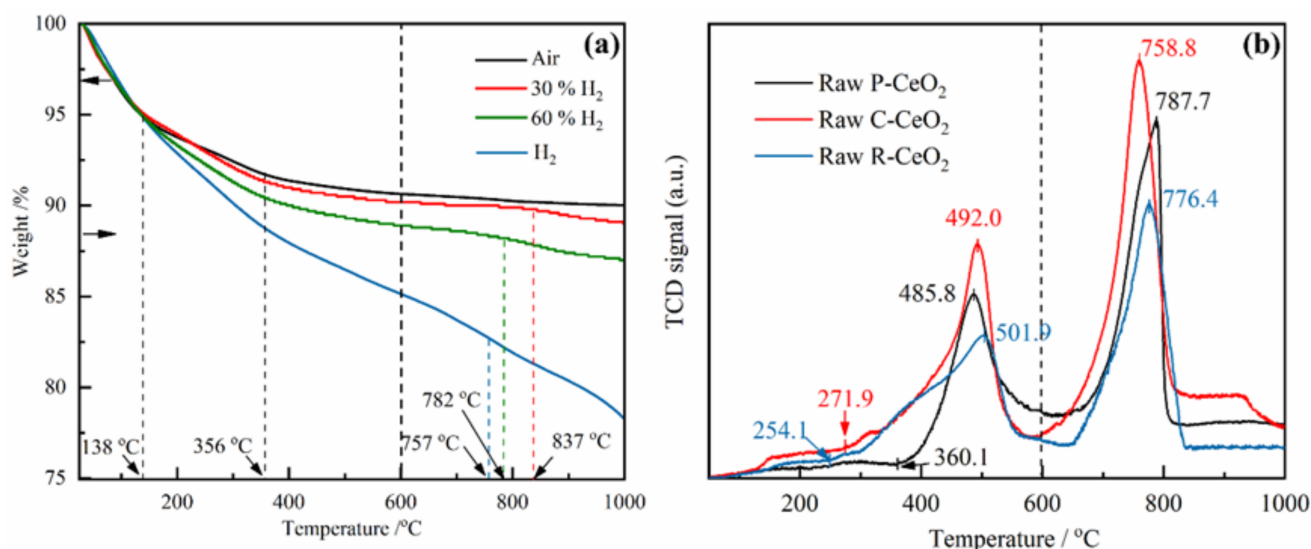


Figure 3. Thermal reduction behavior of synthesized ceria, (a) the thermo-gravimetric analysis of raw R-CeO₂ under different atmosphere, (b) the H₂-TPR of raw P-CeO₂, C-CeO₂ and R-CeO₂.

3.3. OVs Characterization

Three shaped ceria powders were annealed in four types of atmospheres, and different colored products were obtained, where the ceria annealed in air is pale yellow for P-CeO₂ and R-CeO₂, white for C-CeO₂, and then turns to greyish-green or blue-yellow with the increasing of H₂ partial pressure, and the colors of annealed ceria are shown in Figure S2. It is known that the color of pure and stoichiometric cerium dioxide is pale yellow [51], and its color will turn to blue or even black after the formation of nonstoichiometric ceria [52], the observed color variation means an abundance of OVs were generated after hydrogen annealing.

The Ce 3d spectra of raw and annealed ceria are shown in Figure 4, three final states of Ce⁴⁺, including Ce3d⁹4f⁰O2p⁶, Ce3d⁹4f¹Op⁵ and Ce3d⁹4f²O2p⁴ expressed as u''' (v'''), u'' (v'') and u (v) for Ce3d_{3/2}(Ce3d_{5/2}), respectively; two final states of Ce³⁺, including Ce3d⁹4f¹O2p⁶ and Ce3d⁹4f²O2p⁵, are expressed as u' (v') and u₀ (v₀) for Ce3d^{3/2}(Ce3d^{5/2}) [53–56]. The Ce³⁺ fraction was calculated by the following equation [57].

$$\text{Ce}^{3+} / (\text{Ce}^{3+} + \text{Ce}^{4+}) = \text{area}(v_0, u_0, v', u') / \text{total area.} \quad (4)$$

As shown in Figure 4, the areas of v' and u' corresponding to the Ce³⁺ are increasing after annealing in a higher hydrogen contained atmosphere, which means more Ce⁴⁺ in ceria was reduced to Ce³⁺. Calculated Ce³⁺ fractions are shown in Figure 4d, where an obvious rising of Ce³⁺ fraction can be found with the increasing of hydrogen concentration, the Ce³⁺ % increases from 10.66 to 16.56%, 9.71 to 15.12%, and 11.73 to 19.55% for the P-CeO₂, C-CeO₂, and R-CeO₂, respectively. More OVs appear on the surface of R-CeO₂ which is related to the suitable surface activity of (110) facet [58]. In O 1s spectra (are given in Figure S3), oxygen species are originated from lattice oxygen (O_L) attached to Ce⁴⁺ ion and adsorbed oxygen to Ce³⁺ site (O_V), which can be deconvoluted into two peaks at around 529.2 and 531.3 eV, respectively [59,60]. The area and intensity of O_V peak are relevant to the oxygen vacancy in the host lattice, which is calculated and given in Table S2. It can be found that the O_V fraction of ceria increases with the rising of H₂ concentration in annealing gas, which further identified the results shown in Ce 3d spectra that more surface OVs are generated after annealing in a higher H₂ concentration atmosphere at 600 °C.

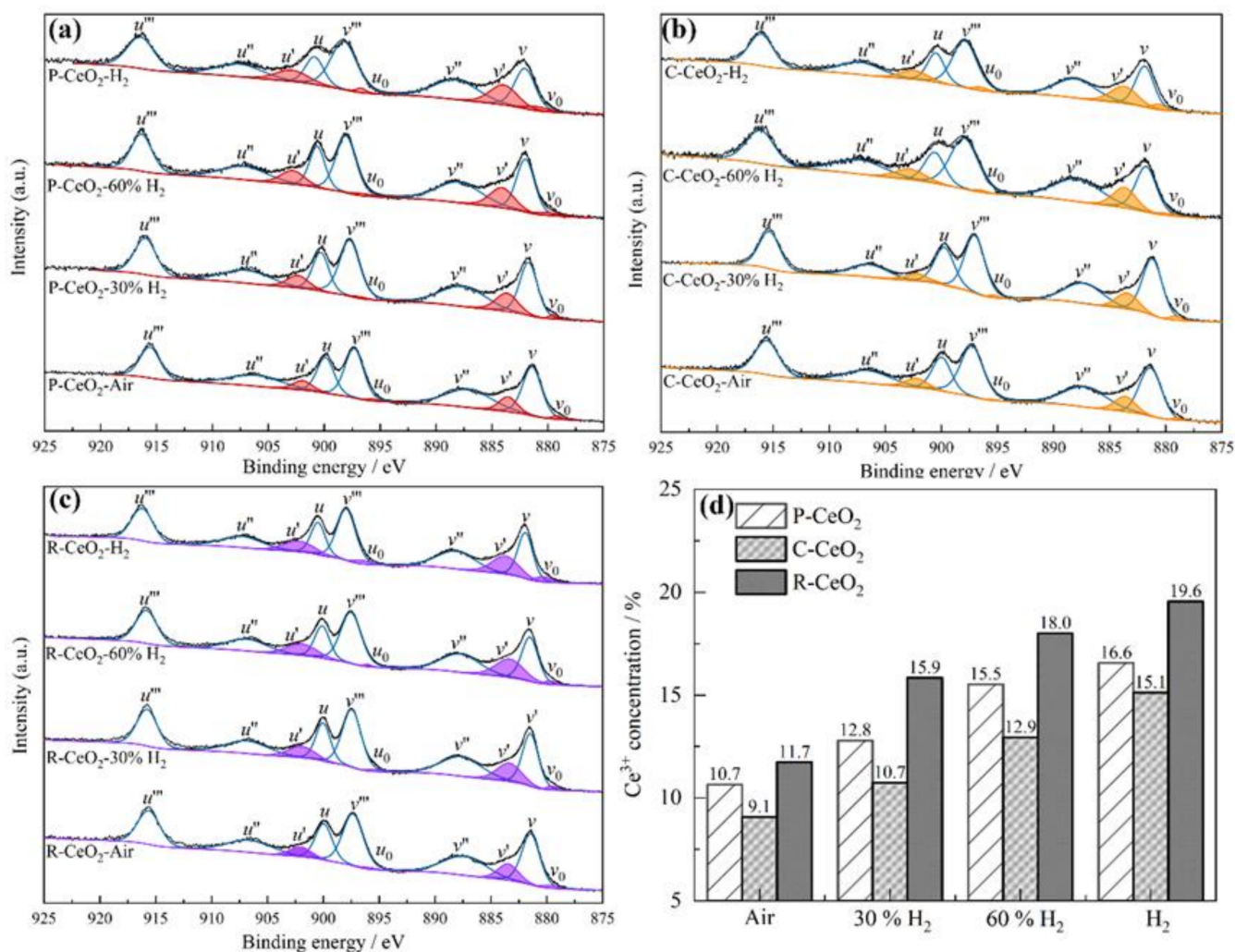


Figure 4. The XPS spectra of P-CeO₂ (a), C-CeO₂ (b) and R-CeO₂ (c) annealed in different concentration of H₂, and the calculated Ce³⁺ fractions (d).

3.4. Photocatalytic Activities

Photocatalytic properties of tested ceria are shown in Figure 5, and the photodegradation ratio of the tested samples is presented in Table S3 together with the calculated degradation rate constants. It is clearly found that the annealed ceria has a higher photocatalytic activity than that of raw material, and the photocatalytic activities of three structural ceria are elevated gradually with the increasing of surface OV concentration. The observed results further verified the reported results [20–22,26] that the OVs are beneficial for the enhancement of photocatalytic property of ceria. P-CeO₂-H₂ has the highest photodegradation ratio of MB of 93.82%, which is larger than 90.09% of R-CeO₂-H₂ and 85.15% of C-CeO₂-H₂. The excellent photocatalytic activity of P-CeO₂ may be due to its smallest average particle size around 9 nm.

As it is known that size [61], morphology [62] and OV concentration [63] are the main factors which influence the photocatalytic activity as well as the photoelectric characterizations of ceria. The TEM images of the CeO₂ annealed in air and pure hydrogen are given in Figures S4–S7. It can be seen that the annealed P-CeO₂ still exhibits (111) facet, the crystal plane of annealed C-CeO₂ is transformed from (100) to stable (111). The plane of calcined R-CeO₂-Air is also tended to (111) with small particles aggregating, but the previously existing (110) facets are turned to active (100) in R-CeO₂-H₂ with the small holes on nanorods. The average particle size of P-CeO₂-H₂ and C-CeO₂-H₂ is larger than that of

P-CeO₂-air, and C-CeO₂-air, respectively, but the length of R-CeO₂-H₂ is found as around 60 nm which is shorter than that of R-CeO₂-air.

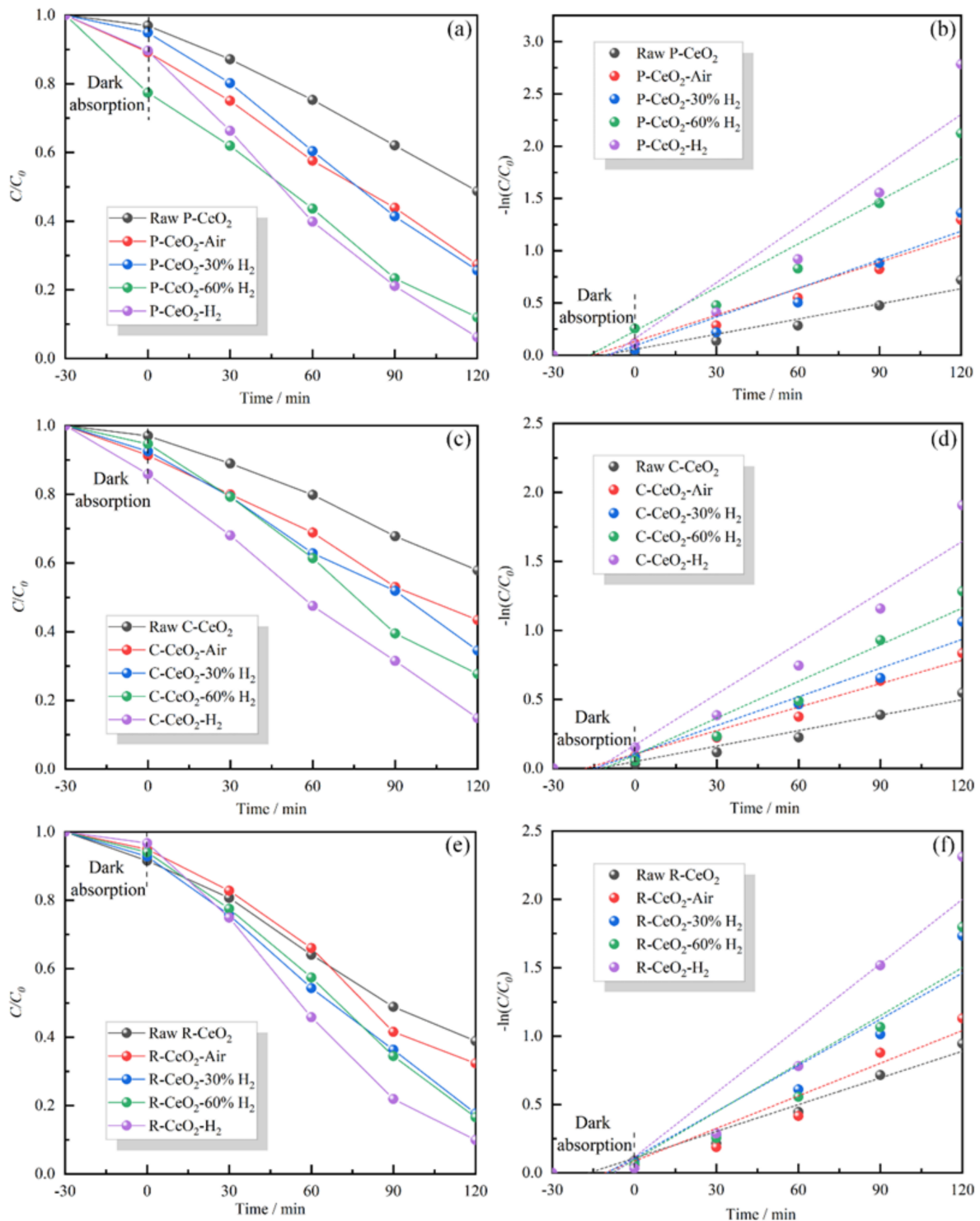


Figure 5. The photocatalytic degradation ratio and rate of P-CeO₂ (a,b), C-CeO₂ (c,d), and R-CeO₂ (e,f) calcining in different atmosphere.

The XRD patterns of C-CeO₂ annealed in air, 30%, 60% and pure H₂ are shown in Figure S8. It can be found that all annealed samples have the similar diffraction pattern of CeO₂, no peaks of Ce₂O₃ can be found. The calculated crystal size is given in Table S4,

the crystal size of the ceria increased after annealing, which is in agreement with the TEM images, while the sample annealed in hydrogen has a slightly increased crystal size compared with that in air. Moreover, the nitrogen adsorption–desorption isotherms of the P-CeO₂, C-CeO₂, and R-CeO₂ calcining in air or pure H₂ are shown in Figure S9. It was calculated that the BET surface area of P-CeO₂-air, C-CeO₂-air and R-CeO₂-air is 60.25, 20.94 and 68.20 m²/g, respectively, where that of P-CeO₂-H₂, C-CeO₂-H₂ and R-CeO₂-H₂ is 10.41, 16.43, and 44.76 m²/g. We found that the BET surface area of all samples decreased after calcining in H₂, which further indicates that the surface OVs concentration is the major factor on the photocatalytic properties of ceria in this study. In addition, the excellent photocatalytic performance of P-CeO₂ may be related to the ordered mesoporous structure.

Hence, the similar morphology, size and BET surface area of the annealed ceria in different atmospheres suggests that the surface OVs concentration is the major factor in the photocatalytic properties of ceria in this study.

3.5. Band Structure of as Prepared Ceria

The UV-Vis DRS spectra and the band energy curves of CeO₂ are shown in Figure 6, and the calculated band gap values are given in Table S5, and it is found that the variations of the light absorption behavior and the band gap for the different morphology ceria before and after annealing are not stereotyped. After annealing, the band gap firstly expands and then slightly narrows with the increase of surface OVs concentration. Raw P-CeO₂ has a band gap of 2.987 eV, while the band gap values of annealed cubic nanoceria are in the range of 2.796–2.864 eV. C-CeO₂ samples have similar band gaps of 3.170–3.204 eV. Raw R-CeO₂ has a narrower band gap of 2.882 eV than that of annealed R-CeO₂ samples, while the band gap value of R-CeO₂-air increases to 3.019 eV and then turns to 3.283 eV for 30% H₂ annealed sample, by continually increasing the H₂ concentration the values tend to decrease slightly. Interestingly, the observed variations of band gap are quite different from the previous reports (e.g., [21,26]), and no significant changes of band gap are observed with the increasing of OVs concentration, which indicates that the surface OVs generated by hydrogen annealing at 600 °C have minimal effects on the band gap of nanoceria.

Band gap energy (E_g) of ceria depends on the conduction band (CB) and valence band (VB), the energy of VB (E_{VB}) of annealed ceria was analyzed by UPS and the results are shown in Figure 7, where the band edge position of CB (E_{CB}) was calculated based on the relationship as given in Equation (5).

$$E_{VB} = E_{CB} + E_g. \quad (5)$$

Moreover, the value of E_{VB} and E_{CB} can be generally calculated by the Mullikan Electronegativity equation [64]:

$$E_{CB} = \chi - E_C - 1 / 2 E_g, \quad (6)$$

where χ is the absolute electronegativity of E_C the semiconductor, the χ value of CeO₂ is reported as 5.56 eV [65], and E_C is the energy of free electrons on the hydrogen scale (−4.5 eV [66]). The measured and calculated E_{VB} and E_{CB} are listed in Table S5, where it can be found that the band edge positions obtained under different conditions present a similar variation trend for the same shaped ceria samples. For three studied structured ceria, the E_{VB} expands to a more positive position when the annealing atmosphere turns to 30% H₂ from air, then decreases with the rising of H₂ concentration. On the contrary, the values of E_{CB} of C-CeO₂ and P-CeO₂ are firstly moved to the Fermi level closely and then become more negative with the OVs concentration rising, while the E_{CB} of R-CeO₂ is firstly expanded to a more negative position and then turns back to Fermi level with the increase of surface OVs.

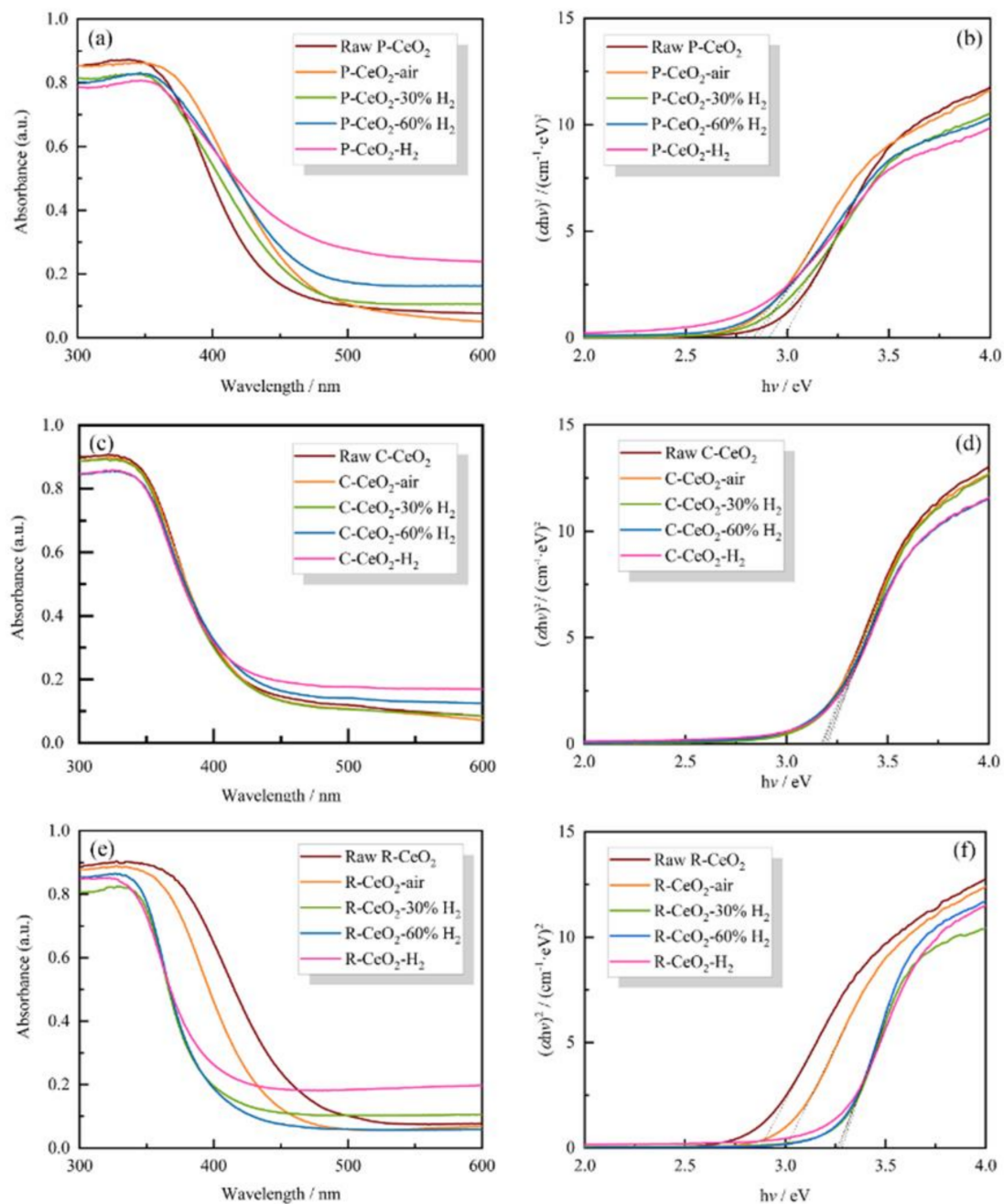


Figure 6. UV-Vis DRS and energy band curves of P-CeO₂ (a,b), C-CeO₂ (c,d) and R-CeO₂ (e,f) calcining in different concentration of H₂.

3.6. Separation/Recombination of e^-/h^+

PL spectra, as shown in Figure 8, were employed to investigate the recombination efficiency of photoinduced electrons and holes, where a lower recombination rate is characterized by a lower PL intensity [17,67]. It can be found that all PL spectra show strong blue emission peaks centered at 430–490 nm, which is associated with the defect levels localized between the Ce 4f and O 2p bands [68–71]. With the rising of surface OV's concentration, the intensities of PL spectra for P-CeO₂ and C-CeO₂ obviously weaken firstly, then decrease slightly. However, the intensities of emission spectra for R-CeO₂ samples are continually weakening with the increasing of OV's concentration, which may offer an evidence for the potential or further reducing of the recombination rate of photogenerated carrier for ceria nanorod with a higher surface OV's concentration. Besides, after annealing in air, 30% and

60% H₂, R-CeO₂ shows a lower PL intensity than that of other typical structure nanocerium, while after annealing in pure hydrogen, the P-CeO₂ exhibits the lowest PL intensity.

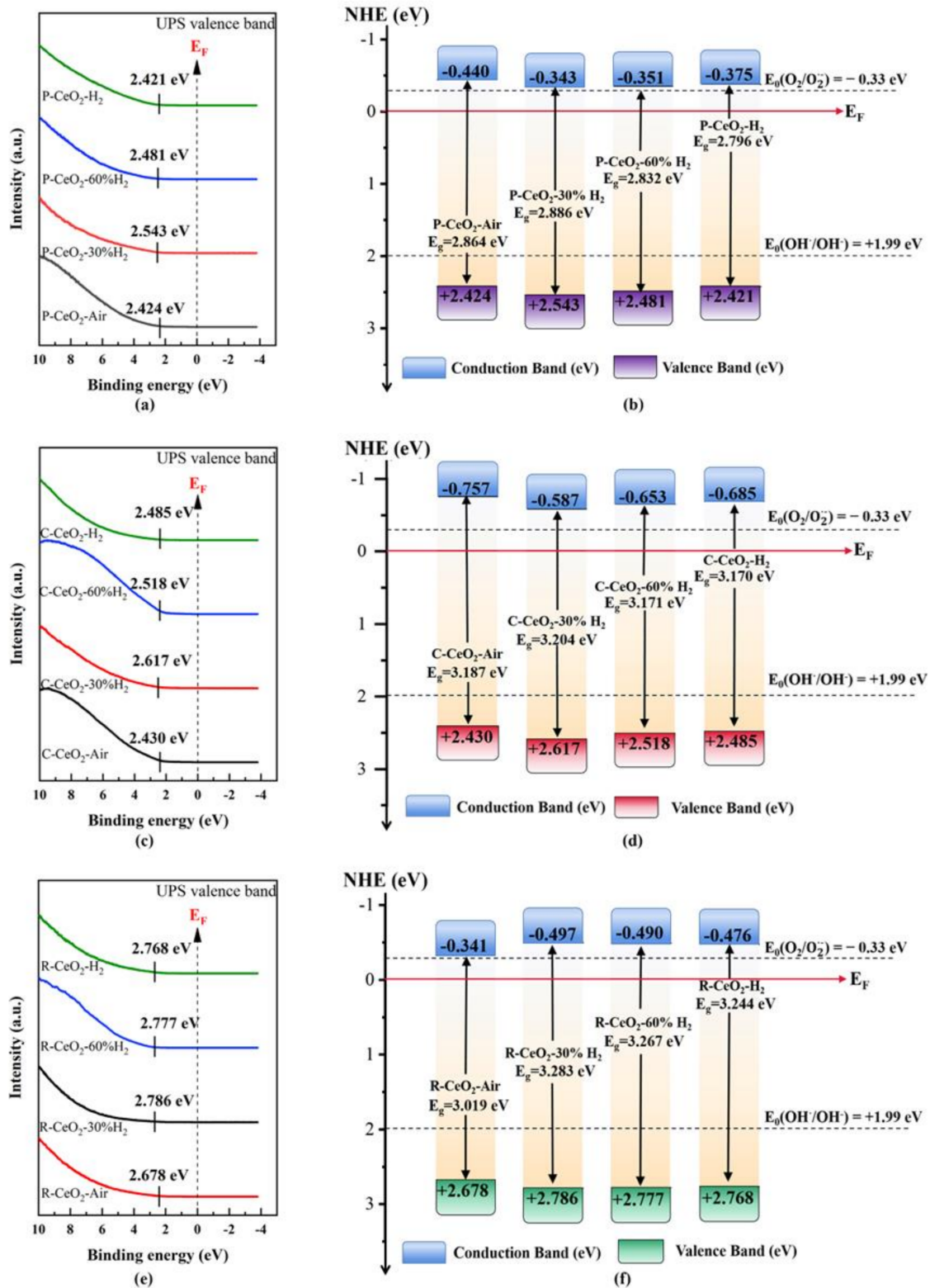


Figure 7. UPS valence band spectra and energy band gap schematic diagram of P-CeO₂ (a,b), C-CeO₂ (c,d), and R-CeO₂ (e,f) annealed in different concentration of H₂.

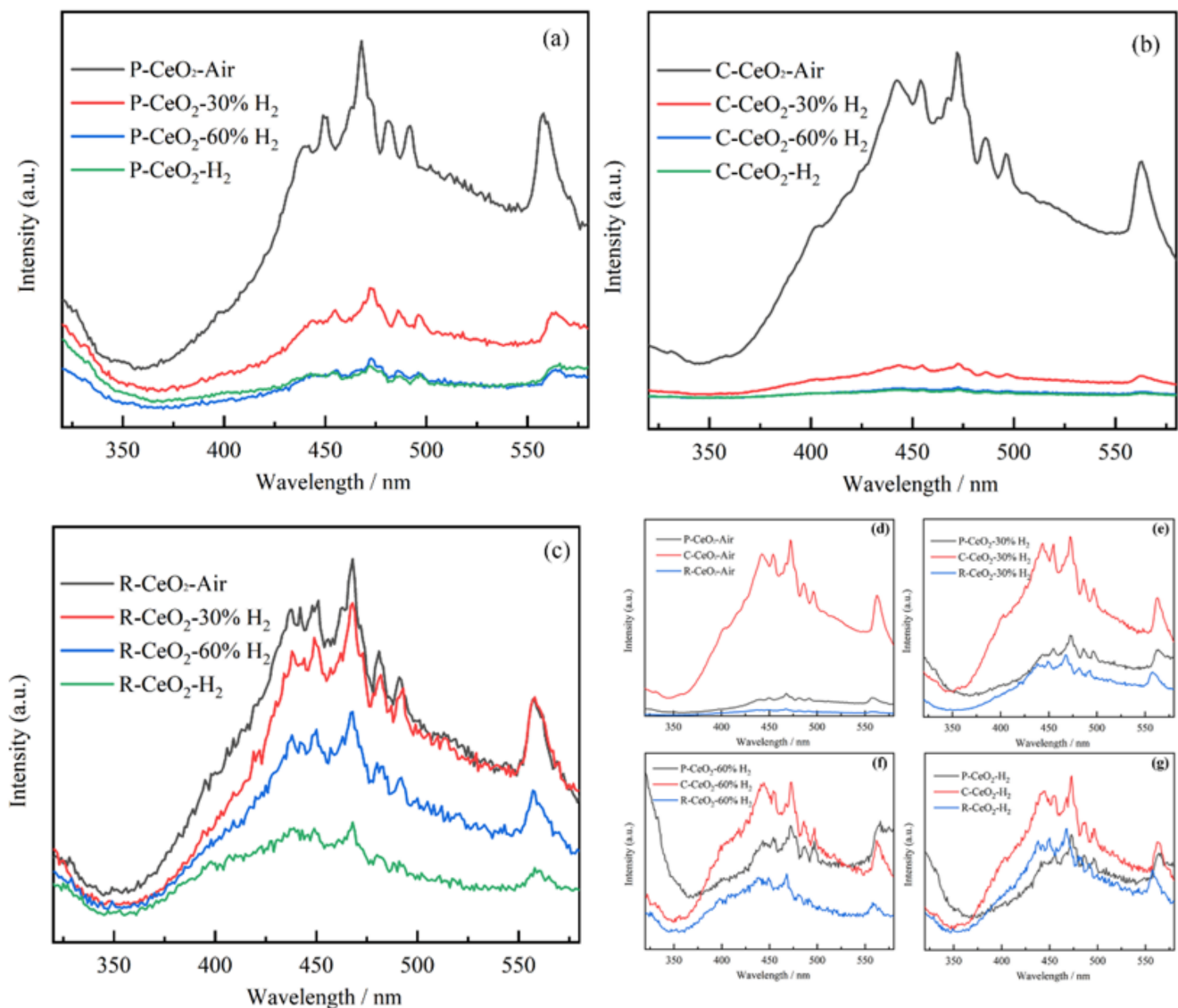


Figure 8. The PL spectra of annealed P-CeO₂ (a), C-CeO₂ (b), R-CeO₂ (c) and the samples annealed in same condition (d–g).

In order to further confirm the separation efficiency of photogenerated electron-hole pairs of the studied samples [72], the transient photocurrent response experiments were measured, and the average photocurrent densities are shown in Figure 9 and Table S6. Higher photocurrent densities are presented with the rising of surface OV concentration in P-CeO₂, C-CeO₂ and R-CeO₂ annealed in increasing concentration of H₂, which suggests a higher surface OV concentration may elevate the e⁻/h⁺ separation efficiency of CeO₂ photocatalyst. It is generally known that a higher separation and lower recombination rate of e⁻/h⁺ are beneficial to the better photocatalytic activity [73], which provide further evidence for the enhancement of photocatalytic activity of ceria after annealing in hydrogen.

3.7. Proposed Mechanism for Photocatalytic Enhancement

To evaluate the contributions of surface OV on the photoelectric characterizations and photocatalytic activity of ceria, the offset values of each property of different hydrogen annealed ceria compared with the air annealed CeO₂ were calculated using the following equation:

$$\text{Offset Value} = (P_i - P_0) / P_0 \times 100\%, \quad (7)$$

where P means the properties including band gap value, photodegradation ratio of MB at 2 h or the photogenerated current, i ($i = 0, 1, 2,$ and 3) represents the number of annealed samples, where 0, 1, 2, and 3 means the sample annealed in air, 30%, 60%, and pure H_2 , respectively.

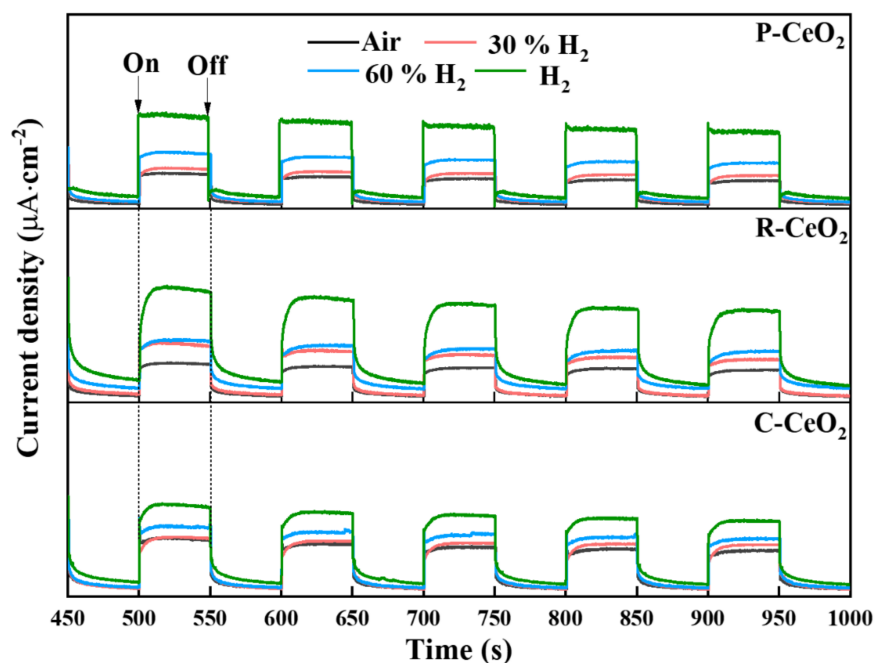


Figure 9. The transient photocurrent curves of P-CeO₂, C-CeO₂ and R-CeO₂ calcining in different concentration of H₂.

The relationships of offset values vs. surface Ce³⁺ concentration of ceria are shown in Figure 10 and Table S7. The offset value of band gap is slightly decreasing with the increasing of surface Ce³⁺ while the 30% H₂ annealed samples have a wider band gap than that of air annealed ceria, suggesting that surface OVs may expand the band gap of ceria firstly, and then the band gap value tends to decrease slightly with a continual rising of surface OVs. Revealed results may explain the reported references, e.g., Gao et al. [22] obtained rich surface OVs ceria by surface engineering with a blue shift of the UV-Vis spectra. Interestingly, the variations both of the offset value of photodegradation ratio and the photocurrent density are notably rising with an increase of surface OVs, which indicates that the reduction of e⁻/h⁺ recombination may be the major contribution of surface OVs on the enhancement of photocatalytic activity under same light source.

Comparing the effects of surface OVs on different shaped ceria, it can be found that surface OVs affect the photocatalytic activity most significantly on the cubic ceria, while C-CeO₂ contains low surface OVs due to its large particle size and high activity of (100) facet, more surface OVs induced in ceria nanocube lattice may result in a moderate photocatalytic activity. Even the effect of surface OVs working on photocatalytic activity of R-CeO₂ is slightly smaller than that of P-CeO₂, but more OVs can be generated in the R-CeO₂, which also results in a high photocatalytic activity. On the other hand, the polyhedral ceria has the smallest size distribution, which may be one of important reasons for its excellent photocatalytic property.

Based on the revealed results, the contributions of surface OVs on the photocatalytic activity of ceria can be concluded as shown in Figure 11. In the range of studied surface OV concentration in cubic, polyhedral or rod-like ceria, a significantly reduction of the combination of e⁻/h⁺ is the major contribution of surface OVs on the promoted photocatalytic activity, while the band gap varies slightly. The surface OVs in CeO₂ lattice are rearranged to produce small microdomains [74] and ordered together to form electron deep

traps which can facilitate the reduction of the recombination rate between photoelectrons and holes during the photocatalytic process [24,75]. Moreover, surface OV's profit the adsorption of O_2 or OH^- on ceria surface, which will promote the generation of radical and reduce the recombination of e^-/h^+ photocarriers [69]. Hence, under the same illumination condition, the photocatalytic activity is obviously enhanced with the rising of surface OV's concentration, which is majorly influenced by the reduced recombination of e^-/h^+ . In addition, the effect rule of surface OV's on photoelectric characterizations and photocatalytic activity of cubic, polyhedral and rod-like ceria is similar but with different incidence, furthermore, reducing particle size and gaining OV's concentration of ceria are still the major tactics for enhancing its photocatalytic activity.

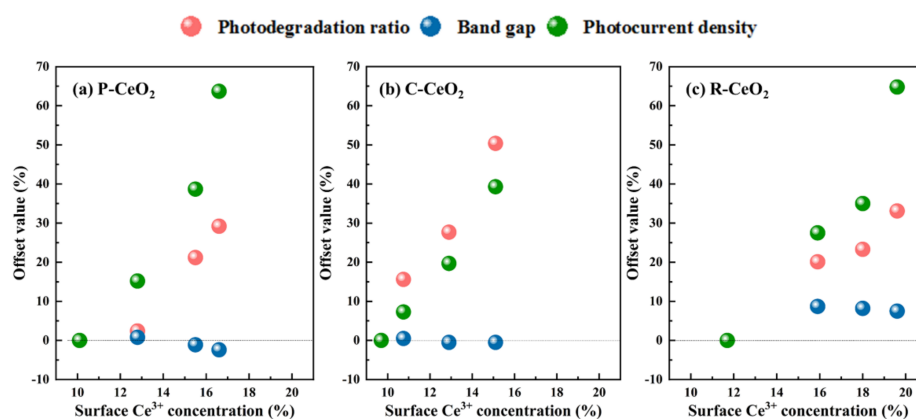


Figure 10. The contributions of Ce^{3+} on the photoelectric characterizations and photocatalytic activity.

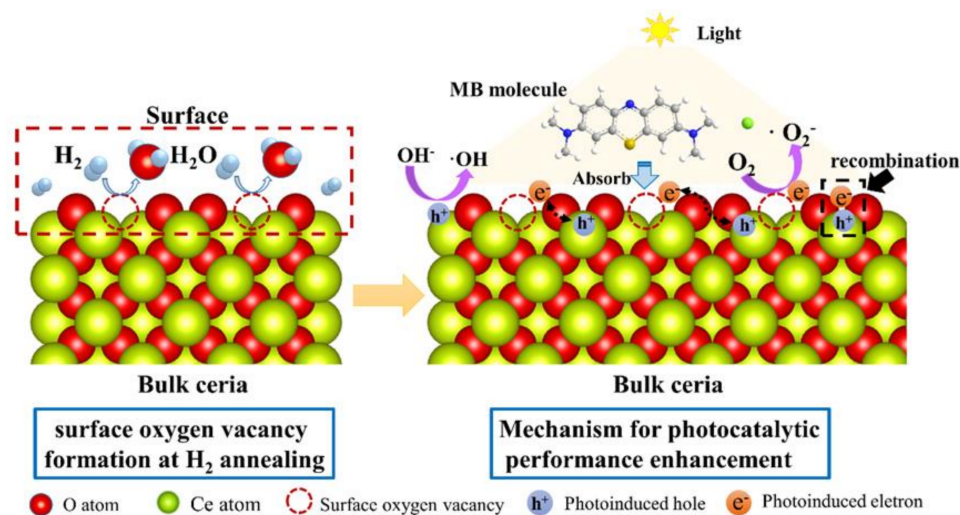


Figure 11. Mechanism schematic of promoted photocatalytic activity of surface contained nanoceria.

4. Conclusions

After sufficient discussion of the revealed results, it can be concluded that a concentration gradient of surface OV's can be generated in ceria lattice after annealing nanoceria at $600^\circ C$ in various H_2 concentration atmospheres, and the ceria annealed in hydrogen has a larger particle size and the exposing lattice face tuned after annealing. Surface OV's significantly enhanced the photocatalytic activity of ceria, the MB degradation ratio after 2 h with pure hydrogen annealed C-CeO₂, P-CeO₂, or R-CeO₂ is 85.15%, 93.82% and 90.09%, respectively, which is 1.5, 1.29 and 1.33 times higher than that of the air annealed sample. The band structure, including band gap, VB, and CB of annealed samples vary slightly, even the surface OV's in ceria lattice changed obviously. Recombination of photoinduced carrier, e^-/h^+ , has a notable reduction with the rising of surface OV's, which is suggested

to be the main contribution for the enhancement of photocatalytic activity of ceria with more surface OVVs.

Supplementary Materials: The following are available online at <https://www.mdpi.com/article/10.3390/nano11051168/s1>, Figure S1. Size distribution of raw P-CeO₂ (a), C-CeO₂ (b) and R-CeO₂ (c). Figure S2. Color variation of P-CeO₂, C-CeO₂ and R-CeO₂ (from left to right) calcining in different atmospheres: (a) raw samples without annealing, (b) air, (c) 30% H₂, (d) 60% H₂, and (e) pure H₂ condition. Figure S3. O 1s spectra of P-CeO₂ (a), C-CeO₂ (b) and R-CeO₂ (c) calcining in different concentration of H₂. Figure S4. TEM images and size distribution of P-CeO₂ calcining in air (a–c) and H₂ (d–f) at 600 °C. Figure S5. TEM images and size distribution of C-CeO₂ calcining in air (a–c) and H₂ (d–f) at 600 °C. Figure S6. TEM images and size distribution of R-CeO₂ calcining in air (a–c) and H₂ (d–f) at 600 °C. Figure S7. TEM images of raw R-CeO₂ (a), R-CeO₂-Air (b) and R-CeO₂-H₂ (c). Figure S8. The XRD patterns of C-CeO₂ annealed in air, 30%, 60% and pure H₂. Figure S9. Nitrogen adsorption–desorption isotherms of the P-CeO₂ (a), C-CeO₂ (b), and R-CeO₂ (c) calcining in air or pure H₂. Table S1. Synthetic conditions of raw P-CeO₂, C-CeO₂ and R-CeO₂. Table S2. Ce³⁺ and absorbed oxygen concentration of P-CeO₂, C-CeO₂ and R-CeO₂ calcining in different concentration of H₂. Table S3. Photocatalytic degradation ratio and rate constants of P-CeO₂, C-CeO₂, and R-CeO₂ calcining in different atmospheres. Table S4. The calculated crystal size of C-CeO₂ annealed in air, 30%, 60% and pure H₂. Table S5. Energy band gap, calculated valence and conductive band, tested valence and conductive band of P-CeO₂, C-CeO₂, and R-CeO₂ calcining in different concentration of H₂. Table S6. Average current density (μA/cm²) of P-CeO₂, C-CeO₂, and R-CeO₂ calcining in different concentration of H₂. Table S7. Offset values of photodegradation ratio, band gap and photocurrent density of different hydrogen annealed ceria.

Author Contributions: Conceptualization, Y.L.; data curation, X.X. and X.M.; formal analysis, Y.L.; investigation, Y.L., X.X., X.M., J.Z. and F.L.; methodology, Y.L.; supervision, J.L. and C.C.; writing—original draft, Y.L.; writing—review and editing, X.X., X.M., D.N., Z.C., J.Z. and F.L. All authors have read and agreed to the published version of the manuscript.

Funding: This research was funded by National Natural Science Foundation of China under Grant No. 51804088 and 52074096, the Talents & Platform Funding from Science & Technology Department of Guizhou Province, China, under the Grant No. (2017)5788 and (2018)5781, the Basic Research Program from Science & Technology Department of Guizhou Province (2020)1Y219 and (2019)1082, and the Cultivation Funding of No. 2019(30) and Doctor Funding of No. (2017)04 supported by Guizhou University are gratefully acknowledged.

Data Availability Statement: Data is contained within the article and supplementary material.

Conflicts of Interest: The authors declare no conflict of interest.

References

1. Reed, K.; Cormack, A.; Kulkarni, A.; Mayton, M.; Sayle, D.; Klaessig, F. Exploring the properties and applications of nanoceria: Is there still plenty of room at the bottom? *Environ. Sci. Nano* **2014**, *1*, 390–405. [[CrossRef](#)]
2. Kašpar, J.; Fornasiero, P.; Graziani, M. Use of CeO₂-based oxides in the three-way catalysis. *Catal. Today* **1999**, *50*, 285–298. [[CrossRef](#)]
3. Jha, A.; Jeong, D.-W.; Jang, W.-J.; Lee, Y.-L.; Roh, H.-S. Hydrogen production from water–gas shift reaction over Ni–Cu–CeO₂ oxide catalyst: The effect of preparation methods. *Int. J. Hydrog. Energy* **2015**, *40*, 9209–9216. [[CrossRef](#)]
4. Gabrovska, M.; Ivanov, I.; Nikolova, D.; Krstić, J.; Venezia, A.M.; Crișan, D.; Crișan, M.; Tenchev, K.; Idakiev, V.; Tabakova, T. Improved Water–Gas Shift Performance of Au/NiAl LDHs Nanostructured Catalysts via CeO₂ Addition. *Nanomaterials* **2021**, *11*, 366. [[CrossRef](#)] [[PubMed](#)]
5. Chueh, W.C.; Falter, C.; Abbott, M.; Scipio, D.; Furler, P.; Haile, S.M.; Steinfeld, A. High-flux solar-driven thermochemical dissociation of CO₂ and H₂O using nonstoichiometric ceria. *Science* **2010**, *330*, 1797–1801. [[CrossRef](#)] [[PubMed](#)]
6. Ackermann, S.; Sauvin, L.; Castiglioni, R.; Rupp, J.L.; Scheffe, J.R.; Steinfeld, A. Kinetics of CO₂ Reduction over Nonstoichiometric Ceria. *J. Phys. Chem. C* **2015**, *119*, 16452–16461. [[CrossRef](#)] [[PubMed](#)]
7. Jasinski, P.; Suzuki, T.; Anderson, H.U. Nanocrystalline undoped ceria oxygen sensor. *Sens. Actuators B Chem.* **2003**, *95*, 73–77. [[CrossRef](#)]
8. Feng, X.; Sayle, D.C.; Wang, Z.L.; Paras, M.S.; Santora, B.; Sutorik, A.C.; Sayle, T.X.; Yang, Y.; Ding, Y.; Wang, X. Converting ceria polyhedral nanoparticles into single-crystal nanospheres. *Science* **2006**, *312*, 1504–1508. [[CrossRef](#)]
9. Yang, J.; Xie, N.; Zhang, J.; Fan, W.; Huang, Y.; Tong, Y. Defect Engineering Enhances the Charge Separation of CeO₂ Nanorods toward Photocatalytic Methyl Blue Oxidation. *Nanomaterials* **2020**, *10*, 2307. [[CrossRef](#)]

10. Mao, X.; Xia, X.; Ning, D.; Li, J.; Chen, C.; Lan, Y.-P. Characterizations and photocatalytic activity of ceria nanoparticles synthesized in KCl–LiCl/KOH–NaOH molten flux from different precursors. *J. Nanoparticle Res.* **2021**, *23*, 69. [[CrossRef](#)]
11. Li, M.; Chen, C.; Xu, L.; Jia, Y.; Liu, Y.; Liu, X. Surface defect-rich ceria quantum dots anchored on sulfur-doped carbon nitride nanotubes with enhanced charge separation for solar hydrogen production. *J. Energy Chem.* **2021**, *52*, 51–59. [[CrossRef](#)]
12. Huang, Z.-Q.; Li, T.-H.; Yang, B.; Chang, C.-R. Role of surface frustrated Lewis pairs on reduced CeO₂ (110) in direct conversion of syngas. *Chin. J. Catal.* **2020**, *41*, 1906–1915. [[CrossRef](#)]
13. Wang, M.; Shen, M.; Jin, X.; Tian, J.; Li, M.; Zhou, Y.; Zhang, L.; Li, Y.; Shi, J. Oxygen vacancy generation and stabilization in CeO_{2-x} by Cu introduction with improved CO₂ photocatalytic reduction activity. *ACS Catal.* **2019**, *9*, 4573–4581. [[CrossRef](#)]
14. Pu, Y.; Luo, Y.; Wei, X.; Sun, J.; Li, L.; Zou, W.; Dong, L. Synergistic effects of Cu₂O-decorated CeO₂ on photocatalytic CO₂ reduction: Surface Lewis acid/base and oxygen defect. *Appl. Catal. B Environ.* **2019**, *254*, 580–586. [[CrossRef](#)]
15. Wang, H.; Guan, J.; Li, J.; Li, X.; Ma, C.; Huo, P.; Yan, Y. Fabricated g-C₃N₄/Ag/m-CeO₂ composite photocatalyst for enhanced photoconversion of CO₂. *Appl. Surf. Sci.* **2020**, *506*, 144931. [[CrossRef](#)]
16. Huang, Y.C.; Wu, S.H.; Hsiao, C.-H.; Lee, A.T.; Huang, M.H. Mild Synthesis of Size-Tunable CeO₂ Octahedra for Band Gap Variation. *Chem. Mater.* **2020**, *32*, 2631–2638. [[CrossRef](#)]
17. Xia, X.W.; Lan, Y.P.; Li, J.Q.; Chen, C.Y.; Mao, X.S. Facile synthesis of nanoceria by a molten hydroxide method and its photocatalytic properties. *J. Rare Earths* **2019**, *38*, 951–960. [[CrossRef](#)]
18. Schmitt, R.; Nanning, A.; Krainis, O.; Korobko, R.; Frenkel, A.I.; Lubomirsky, I.; Haile, S.M.; Rupp, J.L. A review of defect structure and chemistry in ceria and its solid solutions. *Chem. Soc. Rev.* **2020**, *49*, 554–592. [[CrossRef](#)]
19. Pinto, F.M.; Suzuki, V.Y.; Silva, R.C.; La Porta, F.A. Oxygen Defects and Surface Chemistry of Reducible Oxides. *Front. Mater.* **2019**, *6*, 260. [[CrossRef](#)]
20. Ma, R.; Islam, M.J.; Reddy, D.A.; Kim, T.K. Transformation of CeO₂ into a mixed phase CeO₂/Ce₂O₃ nanohybrid by liquid phase pulsed laser ablation for enhanced photocatalytic activity through Z-scheme pattern. *Ceram. Int.* **2016**, *42*, 18495–18502. [[CrossRef](#)]
21. Choudhury, B.; Choudhury, A. Ce³⁺ and oxygen vacancy mediated tuning of structural and optical properties of CeO₂ nanoparticles. *Mater. Chem. Phys.* **2012**, *131*, 666–671. [[CrossRef](#)]
22. Gao, W.; Li, J.; Ma, Y.; Qu, Y. Surface engineering on CeO₂ nanorods by chemical redox etching and their enhanced catalytic activity for CO oxidation. *Nanoscale* **2015**, *7*, 11686–11691. [[CrossRef](#)] [[PubMed](#)]
23. Mao, X.; Xia, X.; Li, J.; Chen, C.; Gu, X.; Li, S.; Lan, Y.-P. Self-assembly of structured CeCO₃OH and its decomposition in H₂ for a novel tactic to obtain CeO_{2-x} with excellent photocatalytic property. *J. Alloy. Compd.* **2021**, *870*, 159424. [[CrossRef](#)]
24. Ansari, S.A.; Khan, M.M.; Kalathil, S.; Nisar, A.; Lee, J.; Cho, M.H. Oxygen vacancy induced band gap narrowing of ZnO nanostructures by an electrochemically active biofilm. *Nanoscale* **2013**, *5*, 9238–9246. [[CrossRef](#)] [[PubMed](#)]
25. Wen, W.; Lou, Z.; Chen, Y.; Chen, D.; Tian, S.; Xiong, Y. Tuning the structural properties of CeO₂ by Pr and Fe codoping for enhanced visible-light catalytic activity. *J. Chem. Technol. Biotechnol.* **2019**, *94*, 1576–1584. [[CrossRef](#)]
26. Yuán, S.; Xu, B.; Zhang, Q.; Liu, S.; Xie, J.; Zhang, M.; Ohno, T. Development of visible light response of CeO_{2-x} with the high content of Ce³⁺ and its photocatalytic property. *ChemCatChem* **2018**, *10*, 1267–1271. [[CrossRef](#)]
27. Padeste, C.; Cant, N.W.; Trimm, D.L. The influence of water on the reduction and reoxidation of ceria. *Catal. Lett.* **1993**, *18*, 305–316. [[CrossRef](#)]
28. Binet, C.; Badri, A.; Lavalley, J.-C. A Spectroscopic Characterization of the Reduction of Ceria from Electronic Transitions of Intrinsic Point Defects. *J. Phys. Chem.* **1994**, *98*, 6392–6398. [[CrossRef](#)]
29. Ansari, S.A.; Khan, M.M.; Ansari, M.O.; Kalathil, S.; Lee, J.; Cho, M.H. Band gap engineering of CeO₂ nanostructure using an electrochemically active biofilm for visible light applications. *RSC Adv.* **2014**, *4*, 16782–16791. [[CrossRef](#)]
30. Rao, M.R.; Shripathi, T. Photoelectron spectroscopic study of X-ray induced reduction of CeO₂. *J. Electron Spectrosc.* **1997**, *87*, 121–126.
31. Qiu, L.; Liu, F.; Zhao, L.; Ma, Y.; Yao, J. Comparative XPS study of surface reduction for nanocrystalline and microcrystalline ceria powder. *Appl. Surf. Sci.* **2006**, *252*, 4931–4935. [[CrossRef](#)]
32. González-Elípe, A.R.; Fernández, A.; Holgado, J.P.; Caballero, A.; Munuera, G. Mixing effects in CeO₂/TiO₂ and CeO₂/SiO₂ systems submitted to Ar⁺ sputtering. *J. Vac. Sci. Technol. A* **1993**, *11*, 58–65. [[CrossRef](#)]
33. Sundaram, K.B.; Wahid, P.F.; Melendez, O. Deposition and X-ray photoelectron spectroscopy studies on sputtered cerium dioxide thin films. *J. Vac. Sci. Technol. A* **1997**, *15*, 52–56. [[CrossRef](#)]
34. Holgado, J.; Munuera, G.; Espinós, J.; González-Elípe, A. XPS study of oxidation processes of CeO_x defective layers. *Appl. Surf. Sci.* **2000**, *158*, 164–171. [[CrossRef](#)]
35. Chen, X.; Liu, L.; Peter, Y.Y.; Mao, S.S. Increasing solar absorption for photocatalysis with black hydrogenated titanium dioxide nanocrystals. *Science* **2011**, *331*, 746–750. [[CrossRef](#)] [[PubMed](#)]
36. Zhu, H.; Qin, Z.; Shan, W.; Shen, W.; Wang, J. Pd/CeO₂-TiO₂ catalyst for CO oxidation at low temperature: A TPR study with H₂ and CO as reducing agents. *J. Catal.* **2004**, *225*, 267–277. [[CrossRef](#)]
37. Lan, Y.P.; Sohn, H.Y. Effect of oxygen vacancies and phases on catalytic properties of hydrogen-treated nanoceria particles. *Mater. Res. Express* **2018**, *5*, 035501. [[CrossRef](#)]
38. Lee, Y.; He, G.; Akey, A.J.; Si, R.; Flytzani-Stephanopoulos, M.; Herman, I.P. Raman analysis of mode softening in nanoparticle CeO_{2-δ} and Au-CeO_{2-δ} during CO oxidation. *J. Am. Chem. Soc.* **2011**, *133*, 12952–12955. [[CrossRef](#)]

39. Zhou, Y.; Chen, A.L.; Ning, J.; Shen, W.J. Electronic and geometric structure of the copper-ceria interface on Cu/CeO₂ catalysts. *Chin. J. Catal.* **2020**, *41*, 928–937. [[CrossRef](#)]
40. Zheng, J.; Zhu, Z.; Gao, G.; Liu, Z.; Wang, Q.; Yan, Y.S. Construction of spindle structured CeO₂ modified with rod-like attapulgite as a high-performance photocatalyst for CO₂ reduction. *Catal. Sci. Technol.* **2019**, *9*, 3788–3799. [[CrossRef](#)]
41. Wang, Z.J.; Gao, Y.Z.; Chabal, Y.J.; Balkus, K.J. Oxidative Dehydrogenation of Cyclohexane and Cyclohexene over Y-doped CeO₂ Nanorods. *Catal. Lett.* **2017**, *147*, 738–744. [[CrossRef](#)]
42. Xia, X.; Li, J.; Chen, C.; Lan, Y.-P.; Mao, X.; Bai, F. Optimal rare-earth (La, Y and Sm) doping conditions and enhanced mechanism for photocatalytic application of ceria nanorods. *Nanotechnology* **2021**, *32*, 195708. [[CrossRef](#)] [[PubMed](#)]
43. Mai, H.X.; Sun, L.D.; Zhang, Y.W.; Si, R.; Feng, W.; Zhang, H.P.; Liu, H.C.; Yan, C.H. Shape-Selective Synthesis and Oxygen Storage Behavior of Ceria Nanopolyhedra, Nanorods, and Nanocubes. *J. Phys. Chem. B* **2005**, *109*, 24380–24385. [[CrossRef](#)]
44. Murali, A.; Lan, Y.P.; Sohn, H.Y. Effect of oxygen vacancies in non-stoichiometric ceria on its photocatalytic properties. *Nano-Struct. Nano Objects* **2019**, *18*, 100257. [[CrossRef](#)]
45. Pouretedal, H.R.; Kadkhodaie, A. Synthetic CeO₂ Nanoparticle Catalysis of Methylene Blue Photodegradation: Kinetics and Mechanism. *Chin. J. Catal.* **2010**, *31*, 1328–1334. [[CrossRef](#)]
46. Liu, B.; Zhao, X.; Terashima, C.; Fujishima, A.; Nakata, K. Thermodynamic and kinetic analysis of heterogeneous photocatalysis for semiconductor systems. *Phys. Chem. Chem. Phys.* **2014**, *16*, 8751–8760. [[CrossRef](#)] [[PubMed](#)]
47. Djuričić, B.; Pickering, S. Nanostructured cerium oxide: Preparation and properties of weakly-agglomerated powders. *J. Eur. Ceram. Soc.* **1999**, *19*, 1925–1934. [[CrossRef](#)]
48. Perrichon, V.; Laachir, A.; Bergeret, G.; Fréty, R.; Tournayan, L.; Touret, O. Reduction of cerias with different textures by hydrogen and their reoxidation by oxygen. *J. Chem. Soc. Faraday Trans.* **1994**, *90*, 773. [[CrossRef](#)]
49. Wu, Z.; Li, M.; Howe, J.; Meyer, H.M.; Overbury, S.H. Probing defect sites on CeO₂ nanocrystals with well-defined surface planes by Raman spectroscopy and O₂ adsorption. *Langmuir* **2010**, *26*, 16595–16606. [[CrossRef](#)]
50. Esch, F.; Fabris, S.; Zhou, L.; Montini, T.; Africh, C.; Fornasiero, P.; Comelli, G.; Rosei, R. Electron localization determines defect formation on ceria substrates. *Science* **2005**, *309*, 752–755. [[CrossRef](#)]
51. Neish, A.C. Preparation of pure cerium salts and the color of cerium oxide. *J. Am. Chem. Soc.* **1909**, *31*, 517–523. [[CrossRef](#)]
52. Mogensen, M.; Sammes, N.M.; Tompsett, G.A. Physical, chemical and electrochemical properties of pure and doped ceria. *Solid State Ion.* **2000**, *129*, 63–94. [[CrossRef](#)]
53. Burroughs, P.; Hamnett, A.; Orchard, A.F.; Thornton, G. Satellite structure in the X-ray photoelectron spectra of some binary and mixed oxides of lanthanum and cerium. *J. Chem. Soc. Dalton Trans.* **1976**, 1686–1698. [[CrossRef](#)]
54. Le Normand, F.; El Fallah, J.; Hilaire, L.; Légaré, P.; Kotani, A.; Parlebas, J.C. Photoemission on 3d core levels of Cerium: An experimental and theoretical investigation of the reduction of cerium dioxide. *Solid State Commun.* **1989**, *71*, 885–889. [[CrossRef](#)]
55. Romeo, M.; Bak, K.; El Fallah, J.; Le Normand, F.; Hilaire, L. XPS Study of the reduction of cerium dioxide. *Surf. Interface Anal.* **1993**, *20*, 508–512. [[CrossRef](#)]
56. Skála, T.; Šutara, F.; Škoda, M.; Prince, K.C.; Matolín, V. Palladium interaction with CeO₂, Sn–Ce–O and Ga–Ce–O layers. *J. Phys. Condens. Matter* **2009**, *21*, 055005. [[CrossRef](#)]
57. Borchert, H.; Frolova, Y.V.; Kaichev, V.V.; Prosvirin, I.P.; Alikina, G.M.; Lukashevich, A.I.; Zaikovskii, V.I.; Moroz, E.M.; Trukhan, S.N.; Ivanov, V.P. Electronic and chemical properties of nanostructured cerium dioxide doped with praseodymium. *J. Phys. Chem. B* **2005**, *109*, 5728–5738. [[CrossRef](#)] [[PubMed](#)]
58. Jiang, D.; Wang, W.; Zhang, L.; Zheng, Y.; Wang, Z. Insights into the Surface-Defect Dependence of Photoreactivity over CeO₂ Nanocrystals with Well-Defined Crystal Facets. *ACS Catal.* **2015**, *5*, 4851–4858. [[CrossRef](#)]
59. Du, H.W.; Wang, Y.; Arandiyani, H.; Scott, J.; Wan, T.; Chu, D.W. Correlating morphology and doping effects with the carbon monoxide catalytic activity of Zn doped CeO₂ nanocrystals. *Catal. Sci. Technol.* **2017**, *8*, 134–138. [[CrossRef](#)]
60. Fan, L.; Wang, K.; Xu, K.; Liang, Z.; Wang, H.; Zhou, S.F.; Zhan, G. Structural Isomerism of Two Ce-BTC for Fabricating Pt/CeO₂ Nanorods toward Low-Temperature CO Oxidation. *Small* **2020**, *16*, 2003597. [[CrossRef](#)] [[PubMed](#)]
61. Khan, S.B.; Faisal, M.; Rahman, M.M.; Akhtar, K.; Asiri, A.M.; Khan, A.; Alamry, K.A. Effect of particle size on the photocatalytic activity and sensing properties of CeO₂ nanoparticles. *Int. J. Electrochem. Sci.* **2013**, *8*, 7284–7297.
62. Yang, X.; Liu, Y.; Li, J.; Zhang, Y. Effects of calcination temperature on morphology and structure of CeO₂ nanofibers and their photocatalytic activity. *Mater. Lett.* **2019**, *241*, 76–79. [[CrossRef](#)]
63. Zhang, Q.; Zhao, X.; Duan, L.; Shen, H.; Liu, R. Controlling oxygen vacancies and enhanced visible light photocatalysis of CeO₂/ZnO nanocomposites. *J. Photochem. Photobiol. A Chem.* **2020**, *392*, 112156. [[CrossRef](#)]
64. Islam, M.J.; Reddy, D.A.; Choi, J.; Kim, T.K. Surface oxygen vacancy assisted electron transfer and shuttling for enhanced photocatalytic activity of a Z-scheme CeO₂–AgI nanocomposite. *RSC Adv.* **2016**, *6*, 19341–19350. [[CrossRef](#)]
65. Wetchakun, N.; Chaiwichain, S.; Inceesungvorn, B.; Pingmuang, K.; Phanichphant, S.; Minett, A.I.; Chen, J. BiVO₄/CeO₂ Nanocomposites with High Visible-Light-Induced Photocatalytic Activity. *ACS Appl. Mater. Interfaces* **2012**, *4*, 3718. [[CrossRef](#)]
66. Issarapanacheewin, S.; Wetchakun, K.; Phanichphant, S.; Kangwansupamonkon, W.; Wetchakun, N. A novel CeO₂/Bi₂WO₆ composite with highly enhanced photocatalytic activity. *Mater. Lett.* **2015**, *156*, 28–31. [[CrossRef](#)]
67. Bakkiyaraj, R.; Balakrishnan, M.; Bharath, G.; Ponpandian, N. Facile synthesis, structural characterization, photocatalytic and antimicrobial activities of Zr doped CeO₂ nanoparticles. *J. Alloy. Compd.* **2017**, *724*, 555–564. [[CrossRef](#)]

68. Syed, K.Y.A.; Balamurugan, A.; Devarajan, V.P.; Subramanian, R. Hydrothermal Synthesis of Gadolinium (Gd) Doped Cerium Oxide (CeO₂) Nanoparticles: Characterization and Antibacterial Activity. *Orient. J. Chem.* **2017**, *33*, 2405–2411.
69. Younis, A.; Chu, D.W.; Kaneti, Y.V.; Li, S. Tuning the surface oxygen concentration of {111} surrounded ceria nanocrystals for enhanced photocatalytic activities. *Nanoscale* **2016**, *8*, 378–387. [[CrossRef](#)]
70. Magdalane, C.M.; Kaviyarasu, K.; Priyadharsini, G.M.A.; Bashir, A.K.H.; Maaza, M. Improved photocatalytic decomposition of aqueous Rhodamine-B by solar light illuminated hierarchical yttria nanosphere decorated ceria nanorods. *J. Mater. Res. Technol.* **2019**, *8*, 2898–2909. [[CrossRef](#)]
71. Kesarla, M.K.; Fuentez-Torres, M.O.; Alcludia-Ramos, M.A.; Ortiz-Chi, F.; Espinosa-González, C.G.; Aleman, M.; Torres-Torres, J.G.; Godavarthi, S. Synthesis of g-C₃N₄/N-doped CeO₂ composite for photo catalytic degradation of an herbicide. *J. Mater. Res. Technol.* **2019**, *8*, 1628–1635. [[CrossRef](#)]
72. Lu, X.; Li, X.; Qian, J.; Miao, N.; Yao, C.; Chen, Z. Synthesis and characterization of CeO₂/TiO₂ nanotube arrays and enhanced photocatalytic oxidative desulfurization performance. *J. Alloy. Compd.* **2016**, *661*, 363–371. [[CrossRef](#)]
73. Yang, C.; Yang, J.; Duan, X.; Hu, G.; Liu, Q.C.; Ren, S.; Li, J.L.; Kong, M. Roles of photo-generated holes and oxygen vacancies in enhancing photocatalytic performance over CeO₂ prepared by molten salt method. *Adv. Powder Technol.* **2020**, *31*, 4072–4081. [[CrossRef](#)]
74. Ikegami, L.T. Oxide ionic conductivity and microstructures of Sm- or La-doped CeO₂-based systems. *Solid State Ion.* **2002**, *154–155*, 461–466.
75. Mao, X.; Xia, X.; Li, J.; Chen, C.; Zhang, J.; Ning, D.; Lan, Y.-P. Homogenously Rare-Earth-Ion-Doped Nanoceria Synthesis in KOH-NaOH Molten Flux: Characterization and Photocatalytic Property. *J. Mater. Eng. Perform.* **2021**. [[CrossRef](#)]